APPLIED SCIENCES AND ENGINEERING

A highly sensitive and selective nanosensor for near-infrared potassium imaging

Jianan Liu[1,2]*, Limin Pan[3]*, Chunfeng Shang[2,4,5,6,7]*, Bin Lu[2], Rongjie Wu[2], Yun Feng[2], Weiyu Chen[2,4], Rongwei Zhang[2], Jiwen Bu[2], Zhiqi Xiong[2,4,8†], Wenbo Bu[1,9†], Jiulin Du[2,4,8†], Jianlin Shi[1†]

Potassium ion (K$^+$) concentration fluctuates in various biological processes. A number of K$^+$ probes have been developed to monitor such fluctuations through optical imaging. However, the currently available K$^+$ probes are far from being sensitive enough in detecting physiological fluctuations in living animals. Furthermore, the monitoring of deep tissues is not applicable because of short-wavelength excitation prevailingly used so far. Here, we report a highly sensitive and selective nanosensor for near-infrared (NIR) K$^+$ imaging in living cells and animals. The nanosensor is constructed by encapsulating upconversion nanoparticles (UCNPs) and a commercial K$^+$ indicator in the hollow cavity of mesoporous silica nanoparticles, followed by coating a K$^+$-selective filter membrane. The membrane adsorbs K$^+$ from the medium and filters out interfering cations. The UCNPs convert NIR to ultraviolet light, which excites the K$^+$ indicator, thus allowing the detection of the fluctuations of K$^+$ concentration in cultured cells and intact mouse brains.

INTRODUCTION

Potassium ion (K$^+$) is the most abundant intracellular cation, which is extremely crucial in various biological processes, including neural transmission, heartbeat, muscle contraction, and kidney function (1). Variations in intracellular or extracellular K$^+$ concentration ([K$^+$]) suggest abnormal physiological functions (2–4) or diseases such as heart dysfunction, cancer, and diabetes (5–8). Therefore, developing effective strategies, especially direct optical imaging methodologies, for monitoring the spatiotemporal dynamics of [K$^+$] fluctuations is greatly valuable.

Several optical probes that are responsive to K$^+$ ions have been reported (9–15). However, these probes are not sensitive enough in detecting [K$^+$] fluctuations at a level of a few millimolar (16) that occur typically under physiological conditions. Furthermore, most current probes are unable to differentiate the small fluctuations of [K$^+$] from those of the accompanying sodium ion ([Na$^+$]) during the transmembrane transportation of K$^+$ by Na$^+$/K$^+$ pumps (17). Although fluorescence lifetime imaging has been used to distinguish K$^+$ from Na$^+$ fluorescence in water solution (18), this technique requires specialized instrumentation and analysis. Besides, most K$^+$ sensors can only be excited by short-wavelength light [e.g., ultraviolet (UV) or visible light] (11), leading to serious scattering and limited penetration depth in living tissues. In contrast, near-infrared (NIR) imaging has unique advantages in imaging deep tissues and provides a plausible alternative (19).

RESULTS

K$^+$ nanosensor design

Here, we report an ultrasensitive and selective K$^+$ nanosensor that is excited by NIR light for in vivo K$^+$ imaging (Fig. 1A). The nanosensor was engineered by encapsulating both upconversion nanoparticles (UCNPs) (20–23) and a commercially available K$^+$ indicator, potassium-binding benzofuran isophthalate (PBFI; fig. S1), into the hollow core of mesoporous silica nanoparticles (MSNs) (24, 25). The UCNPs convert NIR light to UV light that excites the acceptor PBFI via luminescence resonance energy transfer (Fig. 1B). The outer surface of the silica nanoparticles was subsequently shielded with a thin layer of K$^+$-selective filter membrane containing micropores (5.7 Å in diameter). These pores were created from carbonyl oxygen (26) and are structurally similar to the potassium channel of *Streptomyces lividans* (KcsA) (27). The precise structural matching between the K$^+$ and the pore lined by carbonyl groups favors the free transfer of K$^+$ through the membrane pore but prevents other biologically relevant cations from diffusion-through. Although PBFI is less K$^+$-selective against Na$^+$ (28), the nanosensor is highly selective because the encapsulated PBFI can only be accessed by K$^+$ that have diffused into the interior of the nanosensor. Moreover, K$^+$ in the outer solution can be efficiently captured by the filter membrane and subsequently diffuse through the mesopores to reach the PBFI molecules in the hollow cavity; thus, the local [K$^+$] is largely increased within the nanosensor, enabling slight fluctuations in [K$^+$] in the solution to be detected.

Structural characterization

Transmission electron microscopic (TEM) images show that the morphology of the nanoparticles has been well controlled in every step of the nanosensor construction (Fig. 2, A to D, and figs. S2 and S3). The diameter of the shielded nanosensors is 85 ± 2.3 nm, while that

[1]State Key Laboratory of High Performance Ceramics and Superfine Microstructure, Shanghai Institute of Ceramics, Chinese Academy of Sciences, Shanghai 200050, China. [2]Institute of Neuroscience, State Key Laboratory of Neuroscience, CAS Center for Excellence in Brain Science and Intelligence Technology, Chinese Academy of Sciences, Shanghai 200031, China. [3]Department of Chemistry, Seoul National University, Seoul 08826, Republic of Korea. [4]University of Chinese Academy of Sciences, 19A Yu-Quan Road, Beijing 100049, China. [5]Brain Disease and Cognitive Science Research Center, Shenzhen Key Laboratory of Affective and Social Cognitive Science, Shenzhen University, Shenzhen 518060, China. [6]Shenzhen Institute of Neuroscience, Shenzhen 518057, China. [7]Guangdong-Hong Kong-Macao Greater Bay Area Center for Brain Science and Brain-Inspired Intelligence, Guangzhou 510515, China. [8]ShanghaiTech University, 319 Yue-Yang Road, Shanghai 200031, China. [9]Shanghai Key Laboratory of Green Chemistry and Chemical Processes, School of Chemistry and Molecular Engineering, East China Normal University, Shanghai 200062, China.
*These authors contributed equally to this work.
†Corresponding author. Email: forestdu@ion.ac.cn (J.D.); wbbu@chem.ecnu.edu.cn (W.B.); xiongzhiqi@ion.ac.cn (Z.X.); jlshi@mail.sic.ac.cn (J.S.)
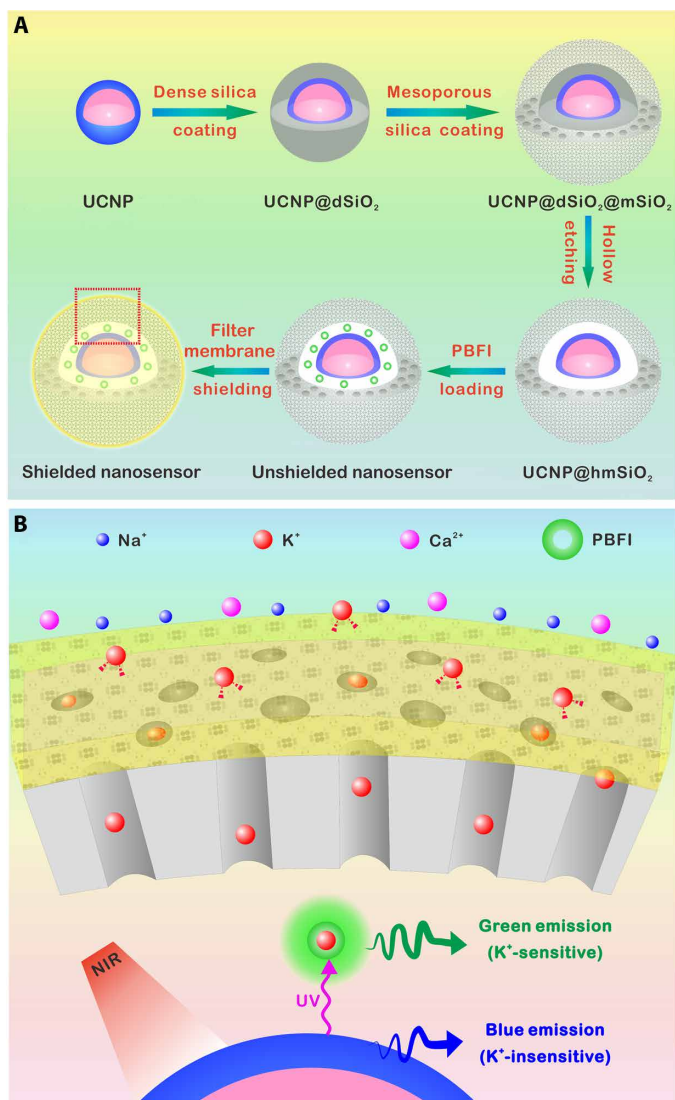
Fig. 1. Design and sensing mechanism of the K⁺ nanosensor. (A) Schematic illustration for the synthesis of the nanosensor. The NaYF₄:Yb/Tm@NaYF₄:Yb/Nd (UCNP) core was synthesized and coated with a dense silica layer and a successive mesoporous silica shell. Etching away of the dense silica layer forms a hollow cavity that allows the loading of PBFI. The nanosensor was lastly coated with the K⁺-selective filter membrane. **(B)** Schematics showing a magnified view of the nanosensor [from the red dotted box in (A)] and its K⁺ sensing mechanism. The filter membrane layer allows only K⁺ to diffuse into and out of the nanosensor, thus excluding the interference from other cations. Once diffused into the nanosensor, K⁺ will bind to PBFI immediately. Upon NIR irradiation, the upconverted UV light from the UCNPs excites PBFI, leading to the emission of K⁺-bonded PBFI.

of the unshielded ones is 81 ± 1.8 nm, indicating a ~2-nm thickness of the filter membrane. Dynamic light scattering and further characterization (fig. S4 and table S1) confirm the presence of the filter membrane on the surface of the shielded nanosensor. Energy-dispersive x-ray spectroscopic (EDS) elemental line scanning of a nanosensor particle (Fig. 2E) dispersed in an aqueous solution (150 mM Na⁺, 150 mM K⁺, 2 mM Ca²⁺, 2 mM Mg²⁺, 50 μM Fe²⁺, 2 mM Zn²⁺, 50 μM Mn²⁺, and 50 μM Cu²⁺) shows that only K⁺ signals can be found in the mesopores and hollow cavities (Fig. 2F), indicating the high shielding effect of the K⁺-specific filter membrane on the nanosensor.
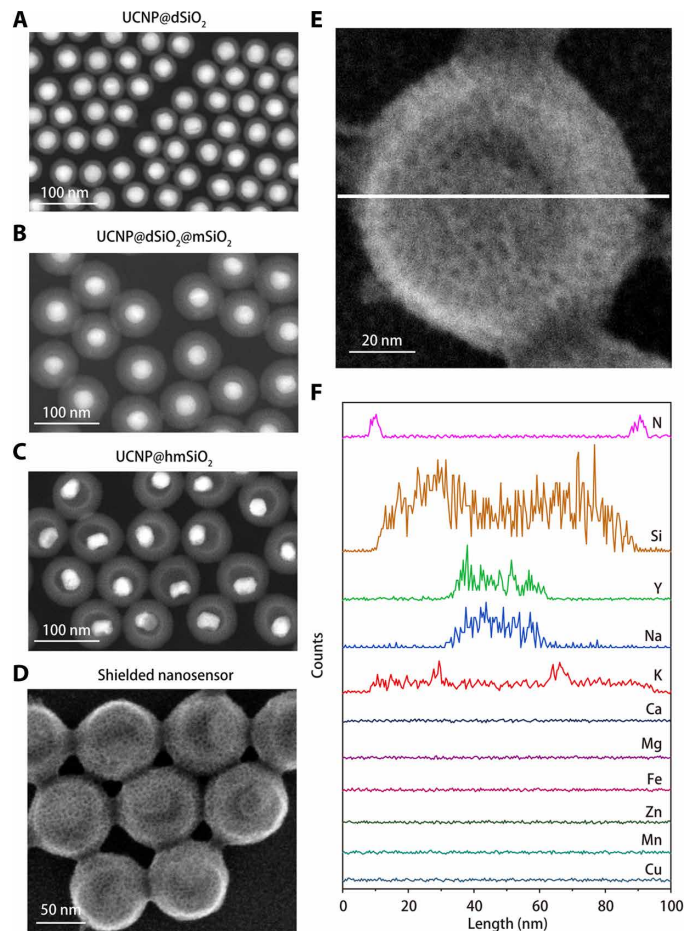
Fig. 2. Structural characterization of the K⁺ nanosensor. (A to C) High-angle annular dark-field images of UCNP@dSiO₂ (A), UCNP@dSiO₂@mSiO₂ (B), and UCNP@hmSiO₂ (C). **(D)** Scanning electron microscopy (SEM) image of the shielded nanosensor. **(E)** SEM image of the shielded nanosensor immersed in an aqueous solution containing 150 mM Na⁺, 150 mM K⁺, 2 mM Ca²⁺, 2 mM Mg²⁺, 50 μM Fe²⁺, 2 mM Zn²⁺, 50 μM Mn²⁺, and 50 μM Cu²⁺. **(F)** EDS elemental line scanning profiles along the white line in (E) reveal that only K⁺ signals are present in the mesopores and hollow cavities of the shielded nanosensors.

Optical K⁺ sensing performance in water solution

The emission peak of the UCNP at 350 nm matches well the maximum absorption band (365 nm) of PBFI, ensuring their efficient luminescence resonance energy transfer (LRET) (Fig. 3A). Upon NIR excitation (808 nm), the shielded nanosensor exhibited three emission peaks at 450, 475, and 540 nm, while the 350-nm emission of the UCNPs disappeared completely, indicating an up to 100% LRET efficiency. In response to the gradual addition of K⁺ into the solution, the shielded nanosensor showed correspondingly enhanced fluorescence intensity at 540 nm, the emission peak of PBFI (Fig. 3B). At the same time, the 450- and 475-nm emissions from UCNPs remained almost unchanged, providing an internal standard of the probe concentration. Furthermore, the ratio of the peak intensities of the 540- and 475-nm emissions is linearly related to [K⁺] (Fig. 3C) but independent of the probe concentration (fig. S5A). These results clearly demonstrate that the shielded nanosensor is capable of quantitatively measuring [K⁺].

We tested whether the shielded nanosensor was sensitive enough to probe [K⁺] in the physiological range of 0 to 150 mM. As [K⁺] increased from 0 to 150 mM, the fluorescence intensity of the shielded
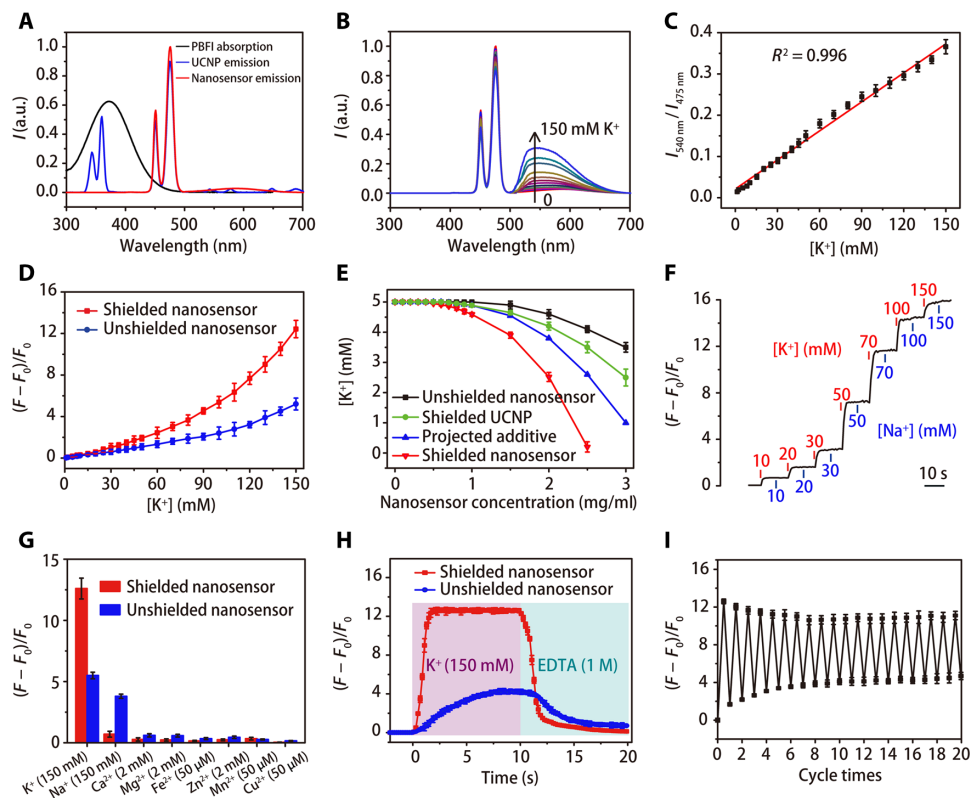
Fig. 3. Spectroscopic features, sensitivity, selectivity, and kinetics of the nanosensor. (**A**) Normalized absorption and emission spectra showing the spectral overlap between the emission of the UCNPs (blue line) and the absorption of the PBFI (black line). The red line is the upconverted emission spectrum of the nanosensor. a.u., arbitrary units. (**B**) [K$^+$]-dependent upconverted luminescence (UCL) spectra of the nanosensor at varied [K$^+$]. (**C**) Intensity ratio of the 540-nm UCL emission to 475-nm emission ($I_{540\,nm}/I_{475\,nm}$) is linearly correlated to [K$^+$]. (**D**) Fluorescence intensities of the unshielded and shielded nanosensors at 540 nm increase by 5- and 12-fold, respectively, in response to [K$^+$] that varies within the physiological range of 0 to 150 mM ($n = 5$). F is the fluorescence intensity at a certain [K$^+$], and F_0 is the emission intensity at 0 mM K$^+$. (**E**) [K$^+$] in aqueous solutions decrease upon application of unshielded, shielded nanosensor, or shielded UCNPs. Initial concentration of K$^+$ in the solutions was 5 mM ($n = 5$). (**F**) Variations in fluorescence intensity of the shielded nanosensor upon stepwise and alternate additions of different concentrations of KCl or NaCl. (**G**) Selectivity of the shielded and unshielded nanosensors toward [K$^+$] against various other physiological cations. (**H**) Time-dependent fluctuations of the nanosensor luminescence intensity upon the addition of K$^+$ and EDTA into the solution. (**I**) Fluorescence intensity of the shielded nanosensor during K$^+$-rich and K$^+$-absent cycles ($n = 5$).

nanosensor increased by more than 12-fold (Fig. 3D). In contrast, the unshielded nanosensor displayed a fivefold fluorescence increase over the same [K$^+$] range. According to the classical theory of Donnan equilibrium, the charged ions near a semipermeable membrane will fail to distribute evenly across the two sides of the membrane. In our case, the filter membrane served as the semipermeable membrane, and MSNs inside the filter membrane were negatively charged; therefore, the nanosensors would attract and concentrate the positively charged ions from the outer solution, which would make the [K$^+$]in higher than [K$^+$]out under equilibrium, as can be confirmed by measuring the local [K$^+$] in the mesopores when the shielded nanosensors were dispersed in the K$^+$-containing solution. We found that the local [K$^+$] in the mesopores were substantially higher than that in the outer solution (fig. S6).

To further determine the mechanism for such an enhanced sensitivity, we added large amounts of unshielded nanosensor or filter membrane–coated UCNP (shielded UCNP) into the solution. Because of the efficient uptake of K$^+$ by the MSNs, the [K$^+$] in the solution decreased substantially (Fig. 3E). In comparison with the unshielded nanosensor, the shielded UCNP and shielded nanosensor show a more substantial decrease in [K$^+$], suggesting that the filter membrane adsorbs K$^+$ more efficiently than mesoporous silica. The ac-

cumulation of K$^+$ increases the local [K$^+$] that is accessible to PBFI. As a result, the shielded nanosensor senses an amplified [K$^+$] in the cavity of the nanosensor, rather than the real [K$^+$] in the outer environment. The detection limit (3σ/slope) of the shielded nanosensor reaches as low as 2.8×10^{-6} M of K$^+$ in the aqueous media, which is sufficient for detecting the submillimolar variation of [K$^+$] in most biological tissues.

In addition to the sensitivity, K$^+$ probes must also be highly selective against Na$^+$. Upon applying Na$^+$ and K$^+$ separately into a solution containing shielded nanosensors, the fluorescence remained highly sensitive to the fluctuations in [K$^+$] but was almost unaffected by the increase in [Na$^+$] (Fig. 3F). The distinctive stepwise profiles of the fluorescent response confirm the superior K$^+$ selectivity of our shielded nanosensor. In the case of the unshielded nanosensor, both 150 mM [K$^+$] and 150 mM [Na$^+$] would lead to substantial fluorescence increases (Fig. 3G). The K$^+$-to-Na$^+$ selectivity ratio of the unshielded nanosensor is as low as 2.6, but in contrast, such a ratio of the shielded nanosensor reaches ~16.1. Examinations in the presence of other physiologically important cations and at pH values resembling the cellular environment (pH 5.5 to 9.0) show that the fluorescence from the shielded nanosensors is sensitive toward neither of them (fig. S5B).

Upon increasing $[K^+]$ from 0 to 150 mM, the fluorescence reached >90% of its maximum within 1 s for the shielded nanosensor (Fig. 3H), whereas 8 s was needed for the fluorescence of the unshielded nanosensors to reach its maximum response. Consistently, when EDTA was introduced to chelate K^+ in the bulk solution, the fluorescence intensity of the shielded nanosensor decreased much faster than that of the unshielded one. These results indicate that the filter membrane containing K^+ affinity sites contributes to the fast kinetics of the shielded nanosensor. Such nanosensors would take several seconds to respond mainly because the negatively charged mesopores tend to bind with K^+ by electrostatic attraction during their diffusion through the mesopore channels into and out of the nanosensor. It is anticipated that the response time will be much shorter if neutral polymers are used instead (29).

We further assessed the reversible performance of the shielded nanosensor under successive K^+-rich and K^+-absent cycles. The signal in K^+-rich conditions remained stable over 20 cycles (Fig. 3I). However, after the first K^+-rich and K^+-absent cycle, the shielded nanosensor showed a moderate signal increase in the K^+-absent condition on the second cycle. The signal intensity in the K^+-absent condition continue to increase slightly over the next 5 cycles before reaching a plateau after 10 adsorption cycles. This increase is due to small amounts of K^+ remaining in the hollow core of the nanosensor. Together, these results demonstrate that the shielded nanosensor is capable of quickly and reversibly responding to the fluctuations of $[K^+]$ within few seconds.

Detection of minor $[K^+]$ fluctuations in cells

Living cells rely on the sodium-potassium adenosine triphosphatase (Na^+/K^+ pump) to maintain a steep $[K^+]$ gradient across their plasma membrane. This gradient is partially responsible for the cell's energy expenditure. Any defect in the metabolism of cellular energy may cause the loss of the $[K^+]$ gradient and the rise in extracellular $[K^+]$ ($[K^+]_o$), resulting in cell death. Decrease in $[K^+]_o$ may also occur when proliferating cells capture K^+ from the culture media to support their growth. The $[K^+]_o$ monitoring offers a valuable indicator of cell viability and growth capabilities. We used the shielded nanosensor to monitor $[K^+]$ fluctuations in living cells. To prevent nonspecific protein adsorption (30) and ensure good colloidal stability, we grafted poly(ethyleneglycol) (PEG) on the surface of the nanosensors (fig. S7). When dispersed in cell culture medium containing human embryonic kidney (HEK) 293 cells, the optical signal of the PEG-modified nanosensors intensified linearly in the positive and negative proportions to cell death and proliferation rates, respectively (fig. S8). In contrast, neither the free organic indicators nor the unshielded nanosensors showed any observable signal variation upon cell death or proliferation, indicating that the shielded nanosensors are fully capable of monitoring $[K^+]$ fluctuations in living cells.

To further improve the sensitivity of the nanosensors, we detected the K^+ efflux immediately after anchoring large numbers of nanosensors onto the cell membrane by targeting streptavidin-conjugated nanosensors to biotin-modified cells (Fig. 4A) (31). HEK 293 cells labeled in this way were treated with a mixture of K^+ efflux stimulators including nigericin, bumetanide (inhibitor of the $Na^+/K^+/2Cl^-$ cotransporter), and ouabain (inhibitor of the Na^+/K^+ adenosine triphosphatase pump). Fluorescence signal (500 to 600 nm) of the membrane-bound shielded nanosensors increased upon this treatment and reached its maximum in around 20 to 30 min before decreasing gradually (Fig. 4B). Comparatively, unshielded nano-

sensors showed much weaker signal responses upon the same treatment (fig. S9). These results demonstrate that the shielded nanosensors are highly sensitive for the continuous monitoring of evoked K^+ efflux.

We further calculated the K^+ efflux rate at different time points of the treatment using a K^+ efflux stimulator. The temporal profile of the calculated K^+ efflux rate matched well with the time-dependent fluorescence variation of both shielded and unshielded nanosensors. However, compared with unshielded nanosensor, the shielded ones show much stronger signal change (Fig. 4C). Furthermore, when the K^+ efflux stimulator was gradually removed, the fluorescence of the shielded nanosensors showed a corresponding decrease, further demonstrating the sensing accuracy (Fig. 4D). Together, the shielded nanosensor is capable of reporting the K^+ efflux rate with much enhanced sensitivity, accuracy, and selectivity.

Optical imaging of spreading waves in the intact mouse brain

We then applied the shielded nanosensors to image cortical spreading depression (CSD) in the mouse brain, which is a wave-like propagation of neural activity. CSD involves a slow propagation of K^+ release in the cortical surface (32). After injecting the PEG-modified shielded nanosensors into the mouse cerebral cortex in a cranial window, CSD events were triggered by KCl incubation in a craniotomy ~3 mm away to avoid interference from such externally applied K^+. We simultaneously monitored the local field potential and the optical signal through the cranial window (Fig. 5A and fig. S9). The increases in nanosensor fluorescence agreed well with electrophysiological CSD events (Fig. 5B). A wave of increasing $[K^+]_o$ propagated gradually across the cortex after the stimulation (Fig. 5, C and D, and movie S1). In comparison, no wave was detected in mice injected with unshielded nanosensors (fig. S9), indicating that the outer filter membrane is crucial to the sensitivity of the nanosensor. By determining the temporal latency of the fluorescence profiles recorded at different locations along the direction of wave propagation, the velocity of the propagation wave was calculated to be 2.9 ± 0.8 mm/min (data are obtained from five mice). This velocity is not significantly different from 3.5 ± 1.1 mm/min ($P > 0.05$, Kolmogorov-Smirnov test), which was determined using blood oxygen level–dependent functional magnetic resonance imaging in patients suffering from migraine aura (33).

Simultaneous monitoring of both K^+ and Ca^{2+} in the zebrafish brain

Neuronal activation is associated with potassium efflux; meanwhile, large increase in extracellular potassium concentration can cause intense neuronal activation, including CSD and epilepsy. In terms of epilepsy, it was found that the impairment of extracellular potassium buffering facilitates the initiation and propagation of epilepsy, suggesting that accumulated extracellular potassium plays an important role in epilepsy occurrence (34, 35). However, there is no direct evidence showing changes in extracellular potassium during epilepsy occurrence. To extend the application of our nanosensor, we thus simultaneously monitored the neuronal calcium activity and extracellular potassium concentration by using zebrafish larvae panneuronally expressing the genetically encoded calcium indicator jRGECO1a and loading its forebrain and midbrain with the potassium nanosensor pneumatically. We applied pentylenetetrazol (PTZ; 20 mM) in bath to induce epilepsy-like neuronal activation (36). Upon
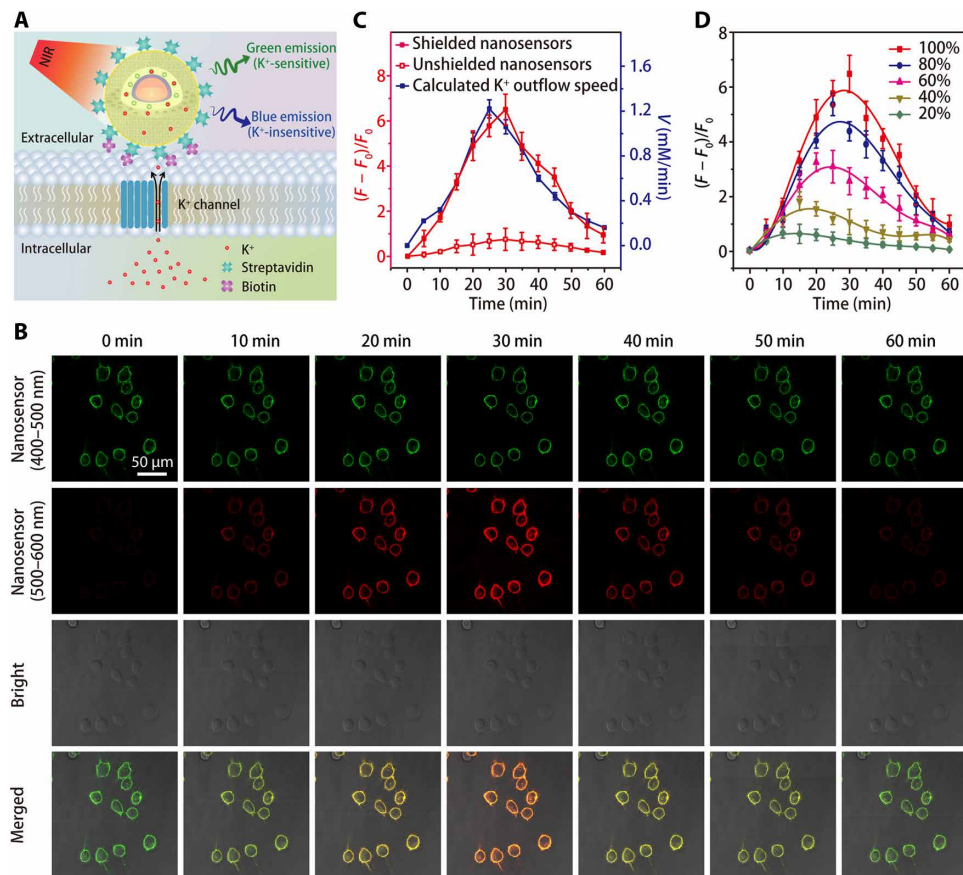
Fig. 4. Imaging of K⁺ efflux in HEK 293 cells. (**A**) Schematics showing the detection of K⁺ efflux by a streptavidin-conjugated nanosensor, which is tethered to a biotin-modified cell. (**B**) Confocal microscopy images showing the fluorescence (at 400 to 500 nm and 500 to 600 nm) of nanosensor-labeled HEK 293 cells at different time points after treatment with the K⁺ efflux stimulator (a mixture of 5 μM nigericin, 5 μM bumetanide, and 10 μM ouabain). (**C**) Time courses of nanosensor fluorescence variations and calculated time dependence of K⁺ efflux rate after treatment with K⁺ efflux stimulator. (**D**) Time-dependent fluorescence fluctuations of shielded nanosensor-labeled HEK 293 cells after treatments with different concentrations (20, 40, 60, 80, and 100%) of K⁺ efflux stimulator. Results from five independent experiments were summarized as mean ± SEM in (C) and (D).

PTZ treatment, both neuronal calcium activity and extracellular potassium concentration increased extensively, as shown by the elevated fluorescence amplitude (Fig. 6A) measured pixel by pixel throughout the imaged brain regions. Epilepsy-like neuronal activities were observed in the anterior optic tectum and the pineal body but not throughout all observed brain areas (Fig. 6A). In contrast, potassium signal appeared in larger brain areas [Fig. 6B, region of interest 2 (ROI2) and ROI3], suggesting that epilepsy-like neuronal activity can lead to increased concentration of extracellular K⁺, which then diffuse to nearby brain regions. Similar results have also been observed on an additional zebrafish larva.

DISCUSSION

A [K⁺] nanosensor with an extremely high sensitivity and selectivity has been constructed by encapsulating UCNPs and a K⁺ indicator in the hollow cores of MSNs, necessarily followed by coating a K⁺-specific filter membrane. The coating of a selective filter membrane largely enhances the selectivity, sensitivity, and kinetics, enabling a rapid and quantitative detection of [K⁺] fluctuations in living cells and intact brains. The filter membrane excludes the interference by other physiological cations and amplifies the [K⁺] signal by increasing the

local [K⁺] in the core of the nanosensor, which enables the detections of extremely low [K⁺] in the surrounding media. It is anticipated that the shielded nanosensor will have broad applications in brain research and improve our understanding of abnormal [K⁺]-related diseases. Advance in enhancing the quantum efficiency of UCNPs (37–39) will further help to improve the imaging depth and in vivo applicability of the shielded nanosensors. Furthermore, the usage of optical fiber–based endoscope and photometry will enable real-time potassium imaging in freely moving animals.

MATERIALS AND METHODS
Materials

YCl₃·6H₂O, YbCl₃·6H₂O, TmCl₃·6H₂O, NdCl₃·6H₂O, oleic acid, 1-octadecene, and dimethyl sulfoxide (DMSO) were purchased from Sigma-Aldrich. Streptavidin, Lipofectamine 3000 reagent, and organic dye DiO for staining phospholipid bilayer membrane were purchased from Thermo Fisher Scientific Co. HCl (37%), methanol, ethanol, and cyclohexane were obtained from Sinopharm Chemical Reagent Co. Phosphate-buffered solution (PBS) (pH 7.4) was obtained from Shanghai Runcheng Biomedical Co. Ltd. All chemicals were obtained commercially and used without further purification.
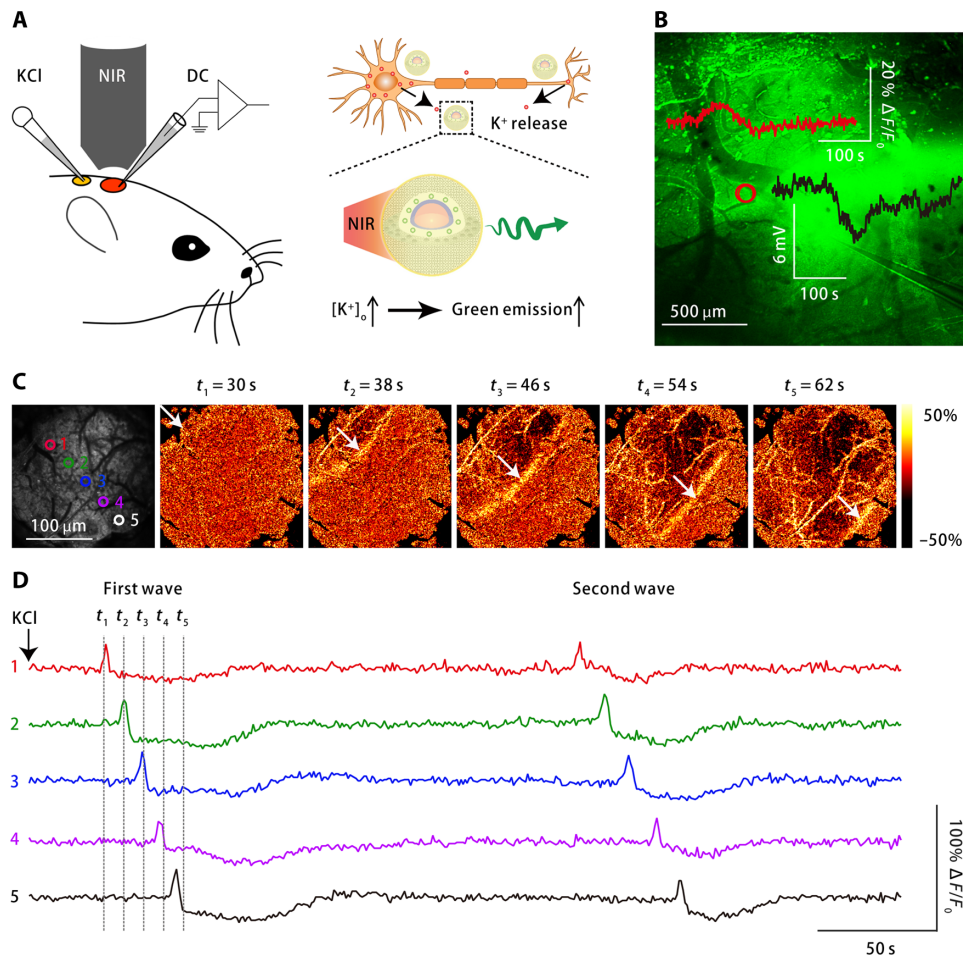
Fig. 5. Nanosensor-assisted imaging of extracellular K$^+$ waves across the cortical surface in a CSD model of mice. (**A**) Schematic of the electrophysiological recording (left) and optical imaging (right) of CSD in the intact mouse brain. Left: The mouse skull was thinned to visualize the cortical surface. CSD was evoked by either KCl incubation or pinprick. A single electrode was inserted to detect CSD by measuring local field potential. Right: CSD-associated K$^+$ release was visualized by detecting the increased fluorescence from the nanosensor. (**B**) Surface fluorescence image showing nanosensor-stained brain parenchyma. Insets show the time courses of the nanosensor's fluorescence signal (red line) at the red region of interest (ROI) and the field potential (black line) recorded near the red ROI. (**C**) Fluorescence images of the brain cortex at the indicated time points after initiating spreading depression. Nanosensor fluorescence is represented as pseudo-color. Color circles represent the locations of the spreading wavefront at different time points after KCl triggering. White arrows depict the direction of the wave propagation. (**D**) Time course of nanosensor fluorescence intensity at the locations indicated by colored circles in (C). Similar results were replicated in five individual mice.

Characterization

TEM images were performed on a JEM-2100F electron microscope operated at 200 kV. Scanning TEM image was acquired on a FEI Magellan 400 electron microscope operated at 30 kV. Hydrodynamic sizes were measured by dynamic light scattering conducted on Zetasizer Nano Series (Nano ZS90). UV-visible spectra were obtained on a UV-3101PC Shimadzu spectroscope. Upconversion luminescence emission spectra were recorded on FluoroLog-3 Spectrofluorometer (Jobin Yvon, France) equipped with an 808-nm semiconductor laser (Beijing Hi-Tech Optoelectronics Co., China). Fourier transform infrared (FTIR) spectroscopy spectra were obtained on a Varian 3100 FT-IR spectrometer. Metal ion concentration was determined by inductively coupled plasma atomic emission spectroscopy (ICP-AES), which were carried out using a Varian Vista-MPX ICP instrument. Fluorescence images were obtained using an Olympus FV1000 upright confocal laser scanning microscope (Olympus, Japan).

Synthesis of UCNPs

NaYF$_4$:Yb (20%)/Tm (0.5%) nanoparticles were synthesized via thermal decomposition method. Typically, 482.3 mg of YCl$_3$·6H$_2$O, 155.0 mg of YbCl$_3$·6H$_2$O, and 2.75 mg of TmCl$_3$·6H$_2$O were dissolved in a mixed solution prepared from 15 ml of oleic acid and 30 ml of 1-octadecene. The resulting solution was directly heated to 156°C under argon atmosphere. This temperature was allowed to maintain for about 1 hour. After the system was cooled down to room temperature, 10 ml of methanol solution containing 296.3 mg of NH$_4$F and 200 mg of NaOH was added. The reaction mixture was kept at room temperature for 2 more hours. After degassing, the solution was heated to 290°C and kept for 1.5 hours. The resulting solution containing oleic acid–capped UCNPs was washed several times with ethanol and redispersed in 20 ml of cyclohexane.

A layer of NaYF$_4$:Yb (10%)/Nd (10%) was grown onto the NaYF$_4$:Yb (20%)/Tm (0.5%) core using a seed-mediated method. Furthermore, 485.3 mg of YCl$_3$·6H$_2$O, 77.5 mg of YbCl$_3$·6H$_2$O, and 71.7 mg of
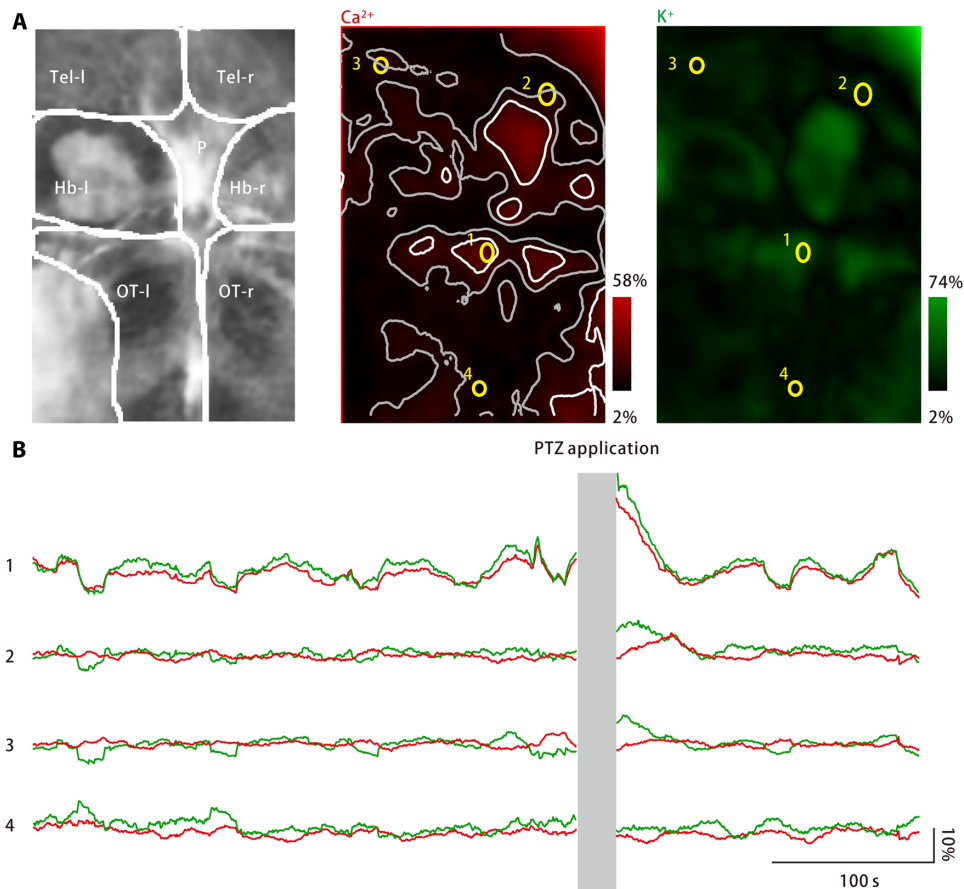
Fig. 6. Extracellular potassium burst in larval zebrafish brain upon PTZ treatment. (**A**) PTZ treatment induced increases in both neuronal calcium activity (middle) and extracellular potassium concentration (right). Left: Imaged brain areas include the left and right telencephala (Tel-l and Tel-r, respectively), the left and right habenulae (Hb-l and Hb-r, respectively), the pineal body (P), and the left and right optic tecta (OT-l and OT-r, respectively). Middle: Neuronal calcium activity was monitored by using a genetically expressed calcium indicator, jRGECO1a. The measured response amplitude is coded in red and mapped back to the imaged brain region. Scattered activity spots are marked as white, and their neighboring zones are marked as gray. Four ROIs (yellow) are selected. Right: Extracellular potassium concentration was monitored by using the potassium nanosensor. The measured response amplitude is coded in green and mapped back to the imaged brain region. (**B**) Neuronal calcium activity (red) and extracellular potassium concentrations observed for the four representative ROIs are marked in (A). After PTZ application, both neuronal calcium activity and extracellular potassium concentration have increased at several activity spots, including the pineal body and the anterior optic tecta, as represented by ROI1. At neighboring zones of the activity spots, neuronal calcium activity change is absent or minimal, while the extracellular potassium concentration continues to increase (ROI2 and ROI3). However, in the area far from the activity spots (ROI4), neither neuronal calcium activity nor extracellular potassium concentration has increased.

$NdCl_3 \cdot 6H_2O$ were dissolved in a mixed solution prepared from 15 ml of oleic acid and 30 ml of 1-octadecene. The resulting solution was heated to 156°C under an argon atmosphere and stirred for 1 hour. After the solution was cooled to room temperature, 10 ml of cyclohexane containing $NaYF_4$:Yb/Tm core nanoparticles was then added into the solution. After degassing, 10 ml of methanol solution containing 296.3 mg of NH_4F and 200 mg of NaOH was added and kept at room temperature for 2 hours. After degassing, the reaction solution was directly heated to 280°C and kept for 1.5 hours. The resulting nanoparticles were washed several times with ethanol and redispersed in 20 ml of cyclohexane.

Synthesis of UCNP@dSiO$_2$

UCNP@dSiO$_2$ was synthesized via water-in-oil reverse microemulsion. One milliliter of Igepal CO-520 was dispersed in 20 ml of cyclohexane and stirred for 30 min. Two milliliters of cyclohexane solution containing UCNP was then added into the mixture. Subsequently, 140 μl of ammonia (30%) was added dropwise and stirred

for 2 hours. Last, by using a syringe pump (WZS-50F6), 200 μl of tetraethyl orthosilicate (TEOS) was slowly introduced into the reaction system with a speed of 200 μl/hour. After keeping magnetic stirring for 24 hours, the resulting products were washed three times with ethanol and dispersed in 20 ml of deionized water (DI H_2O).

Synthesis of UCNP@dSiO$_2$@mSiO$_2$

Ten milliliters of water containing UCNP@dSiO$_2$ was added into the mixed solution containing 20 ml of DI H_2O, 2 g of cetyltrimethylammonium chloride (CTAC), and 0.02 g of triethanolamine (TEA). The solution was heated to 80°C and kept for 1 hour before 0.3 ml of TEOS was added. After reaction for 1 hour, the products were washed three times with ethanol and redispersed in ethanol. To extract the CTAC, the collected products were added into methanol solution containing 1 weight % of sodium chloride (NaCl) and stirred for 3 hours at room temperature. This procedure was repeated four times to completely remove CTAC. Last, the nanoparticles were dispersed in 10 ml of DI H_2O.

Synthesis of UCNP@hmSiO$_2$

UCNP@hmSiO$_2$ was synthesized by selectively etching dense silica layer of UCNP@dSiO$_2$@mSiO$_2$ using a "surface-protected hot water etching" method. Ten milliliters of DI H$_2$O containing UCNP@dSiO$_2$@mSiO$_2$ was added into 10 ml of DI H$_2$O containing 0.25 g of polyvinyl pyrrolidone (M_w = 40,000). After stirring for 0.5 hours, solution was then heated to 95°C and kept for 2.5 hours. After the system was cooled down to room temperature, the resulting nanoparticles were washed three times with ethanol and dispersed in 10 ml of DI H$_2$O.

Synthesis of the shielded nanosensors

First, filter membrane precursors were prepared as follows: 3.4 g of *N*-benzylsalicylamide and 2.5 g of anhydrous potassium carbonate were added into 25 ml of dry dimethylformamide. The resulting mixture was heated to 90°C. Subsequently, 2.9 g of 1,1,1-tris(*p*-tosyloxymethyl)ethane and 0.3 ml of 2-aminoterephthalic acid were added into the solution and stirred for 12 hours. After the solution was cooled to room temperature, the reaction mixture was added into 200 ml of DI H$_2$O. By using petroleum ether-ethyl acetate (2:1) as eluent, the resulting solid products were treated with column chromatography on silica gel to furnish filter membrane precursor as a white solid.

By an in situ loading procedure, the filter membrane precursor was deposited onto the surface of UCNP@hmSiO$_2$-PBFI directly from an acetonitrile solution. Ten milliliters of acetonitrile solution containing 1 mg of filter membrane precursor was added into 50 ml of acetonitrile ultrasonic suspension of UCNP@hmSiO$_2$-PBFI (50 mg) under vigorous stirring. The mixture was kept at 50°C for 10 min, followed by annealing at room temperature for 12 hours. The obtained nanoparticles were washed three times with DI H$_2$O and dispersed in 10 ml of DI H$_2$O.

Adsorption of PBFI in the hollow cavity of UCNP@hmSiO$_2$

One milliliter of UCNP@hmSiO$_2$ (50 mg) and 10 ml of PBFI (0.5 mg/ml) in DI H$_2$O were mixed, and the suspension was stirred for 24 hours at room temperature. The resulting nanoparticles were washed three times with DI H$_2$O. The amount of adsorbed PBFI was determined by comparing the starting amount of PBFI and the remaining amount of free PBFI. The loading amount of PBFI on UCNP@hmSiO$_2$ was calculated as follows: $(M_{initial} - M_{remain})/(M_{initial} - M_{remain} + M_{UCNP@hmSiO2})$.

PEG-modified nanosensor for extracellular sensing

The filter membrane–shielded nanosensor dispersed in DI H$_2$O was activated with *N*-hydroxysuccinimide (NHS)/1-ethyl-3-(3-dimethylaminopropyl)carbodiimide hydrochloride (EDC) for 30 min at pH 5.6 [1 mg of nanosensors in 1 ml of NHS (10 mM) and EDC (10 mM) solution]. Then, 5 mg of monofunctional amine-terminated PEG (M_w = 5000) dissolved in 1 ml of 10 mM NHS/EDC at pH 8.6 was added and mechanically stirred overnight. The modified nanosensors were thereafter purified by three rounds of DI H$_2$O washing. PEG-modified nanosensors were dispersed in DI H$_2$O at 200 mg/ml for further use.

Streptavidin-modified nanosensor for membrane sensing

Ten micrograms of streptavidin, 5 mg of EDC, and 2.6 mg of NHS were added into 4 ml of H$_2$O. The resulting mixture was allowed to stir gently in the dark for 1 hour. Then, 4 ml of DI H$_2$O containing 10 mg of shielded nanosensor was added into the solution. After stirring for 4 hours, the as-synthesized nanoparticles were washed three times with DI H$_2$O and dispersed in DI H$_2$O.

Determination of response time

Nanosensors (3 mg) were dispersed in DI H$_2$O (3 ml). The recording of response data is stated at $t < 0$ s, under the assumption of steady state. At $t = 0$ s, 333 μl of a concentrated water solution containing KCl (1500 mM) was injected into the solution. At $t = 10$ s, 370 μl of a concentrated water solution containing EDTA (10 M) was injected into the solution. During the entire period, nanosensors were exposed to 808-nm NIR light, and their fluorescence intensities were recorded.

Determination of the detection limit

The detection limit of the nanosensor was determined as the following equation

$$\text{Detection limit} = 3\sigma/k$$

where σ is the SD of blank measurement by measuring fluorescence emission spectrum of the nanosensor five times and k is the slope of the linear fit of the fluorescence intensity ratio $F_{540\,nm}/F_{475\,nm}$ against [K$^+$].

Cell culture

HEK 293 cell lines were obtained from the Institute of Biochemistry and Cell Biology, Shanghai Institutes for Biological Sciences, Chinese Academy of Sciences (China). Cells were cultured in Dulbecco's modified Eagle's medium supplemented with 10% fetal bovine serum (FBS) at 37°C under 5% CO$_2$.

Cell cytotoxicity assay by an MTT protocol

To test the cytotoxicity of nanosensors, we anchored the HEK 293 cells with different amounts of nanosensors by incubating HEK 293 cells with varied concentrations of nanosensor (5, 10, 20, 50, and 100 μg/ml). Afterward, 100 μl of culture media containing 50 μg of MTT [3-(4,5-dimethylthiazol-2-yl)-2,5-diphenyltetrazolium bromide] was added. After 4-hour incubation, the cultured medium was extracted, and 100 μl of DMSO was added per well. The absorbance intensity at 490 nm was monitored using a microplate reader (Bio-Tek ELx800).

ICP for quantification of intracellular [K$^+$]

After HEK 293 cells were incubated with a mixture of nigericin, bumetanide, and ouabain for several different durations (5, 10, 15, 20, 25, 30, 35, 40, 45, 50, 55, and 60 min), the cells were harvested by trypsinization. After cell number counting, the cells were washed twice with external solution. Then, the cells were immersed with 3 ml of cell lysis solution (0.5% Triton X-100 and 1 M NaOH), which can totally disrupt the cells with the aid of ultrasound. The masses of K$^+$ in the HEK 293 cells were measured by ICP-AES. Last, [K$^+$] in each cell before and after incubation with nigericin, bumetanide, and ouabain can be accurately calculated.

Cell surface biotinylation and labeling with the nanosensor

First, the cells were transfected with acceptor peptide-transmembrane domain (AP-TM) for further biotinylation. Lipofectamine 3000 Reagent (0.75 μl) was diluted in Opti-MEM Medium (25 μl). In the

meantime, master mix was prepared by diluting AP-TM (1 μg) in Opti-MEM Medium (50 μl) containing P3000 (2 μl). Then, the diluted AP-TM was added in the diluted Lipofectamine 3000 Reagent. The resulting mixture was incubated for 10 min at room temperature. Last, this mixture was mixed with 1 ml of the cell culture medium, and the resulting mixture was allowed to be incubated with cells for 1 day at 37°C.

After incubation for 1 day, cells were washed two times in PBS (pH 7.4). Subsequently, 1 ml of PBS containing the *E. coli* protein–biotin ligase (BirA) (0.3 μM), biotin (10 μM), and adenosine triphosphate (1 mM) was added for the biotinylation of cells. After 10-min incubation at room temperature, the cells were washed two times with PBS. Last, the cells were incubated with 1 ml of PBS containing streptavidin (100 μg/ml)–modified nanosensors for 5 min at room temperature to obtain the nanosensor-anchored cells.

Nanosensor-assisted cell death and proliferation assay

For cell death assay, HEK 293 cells with ~80% confluency were incubated with culture medium/10 mM 2-deoxyglucose/30 μM digitonin. At varied time points, the extracellular [K⁺] was determined by measuring the nanosensor fluorescence intensity upon 808-nm excitation. Morphological observation of HEK 293 cells was performed at an inverted fluorescence microscope.

For cell proliferation assay, HEK 293 cells with ~10% confluency were incubated with culture medium containing 5, 10, 15, or 20% FBS. Nuclear count was performed using a ×20 magnification objective. At varied time points, the extracellular [K⁺] was determined by measuring the nanosensor fluorescence intensity upon 808-nm excitation.

Monitoring the intracellular K⁺ efflux using the nanosensor

HEK 293 cells were labeled with the shielded/unshielded nanosensors as above and observed using a confocal laser scanning microscope (FluoView FV1000, Olympus). Potassium efflux was triggered using a mixture of nigericin (5 μM), bumetanide (10 μM), and ouabain (10 μM) applied in the cell culture medium. Different dilutes (20, 40, 60, and 80%) of the mixture were also used to generate the K⁺ efflux of different degrees.

Potassium imaging in the intact brain of mice

Wild-type C57 mice (20 to 30 g body weight, older than 2 months) of normal phenotype were used. All the experimental procedures were approved by the Institutional Animal Care and Use Committee of the Institute of Neuroscience, Chinese Academy of Sciences. Mice were anesthetized with urethane (120 mg/kg, intraperitoneally) and head-restrained in a standard mouse stereotactic frame. The body temperature was maintained at 36° to 37°C using a heating pad. Four hundred microliters of nanosensors (dispersed in external solution, 100 μg/ml) was injected into cerebellar granule layer (250 to 300 μm from the surface) through a cranial window with a glass pipette using Picospritzer (Parker Hannifin, Hollis, NH, USA). A small craniotomy for KCl stimulation was located ~2 mm away from the cranial window. Optical imaging was performed 1 hour after successful loading of the nanosensors. Fluorescence was collected by using a 40× objective, and a filter set was designed for the nanosensors under 808-nm excitation from a pulsed infrared laser. Full-field images were obtained every 0.88 s. We collected imaging data in two trials for each animal: a basal trial lasting 120 s and a stimulation trial lasting 300 s. Stimulus (1 M KCl) was applied on the surface of the cerebellar cortex at the beginning of stimulation trial. We analyzed the images with ImageJ software.

Monitoring of neuronal activities and potassium levels in the zebrafish brain

The nanosensors were excited by using infrared laser (808 nm, Chameleon Vision, Coherent). Using the fishline huc:NES-jRGECO1a, the neuronal calcium activity was observed through the genetically encoded calcium indicator, jRGECO1a, which was excited by the same laser through two-photon excitation. Their emitted fluorescence was collected by a plan fluorite physiology objective (N20X-PFH, Olympus) and relayed to the detection lightpath of a confocal/two-photon light scanning fluorescence microscope (FV1000, Olympus) using two separate GaAsP photomultiplier tubes. We imaged these channels simultaneously at 2.5 Hz with a pixel dwelling time of 2 μs. We quantified the fluorescence dynamics both in a pixel-by-pixel manner on the rigid-body registered and locally smoothed (5-pixel Gaussian filter) images and for manually segmented neurons, inferring the basal fluorescence at each point using a 20% order filter spanning a time window of 80 s. Fluorescence from badly registered frames was obtained by Piecewise Cubic Hermite Interpolating Polynomial method based on the other frames. The response amplitude was measured as the maximal change in a 36-s window following the PTZ application. All analyses were performed using ImageJ (National Institutes of Health) and MATLAB (MathWorks).

REFERENCES AND NOTES

1. W. O. Fenn, The role of potassium in physiological processes. *Physiol. Rev.* **20**, 377–415 (1940).
2. J. N. Itri, S. Michel, M. J. Vansteensel, J. H. Meijer, C. S. Colwell, Fast delayed rectifier potassium current is required for circadian neural activity. *Nat. Neurosci.* **8**, 650–656 (2005).
3. J. Aqvist, V. Luzhkov, Ion permeation mechanism of the potassium channel. *Nature* **404**, 881–884 (2000).
4. P. Kofuji, E. A. Newman, Potassium buffering in the central nervous system. *Neuroscience* **129**, 1045–1056 (2004).
5. S. K. Vodnala, R. Eil, R. J. Kishton, M. Sukumar, T. N. Yamamoto, N.-H. Ha, P.-H. Lee, M. Shin, S. J. Patel, Z. Yu, D. C. Palmer, M. J. Kruhlak, X. Liu, J. W. Locasale, J. Huang, R. Roychoudhuri, T. Finkel, C. A. Klebanoff, N. P. Restifo, T cell stemness and dysfunction in tumors are triggered by a common mechanism. *Science* **363**, eaau0135 (2019).
6. R. Eil, S. K. Vodnala, D. Clever, C. A. Klebanoff, M. Sukumar, J. H. Pan, D. C. Palmer, A. Gros, T. N. Yamamoto, S. J. Patel, G. C. Guittard, Z. Yu, V. Carbonaro, K. Okkenhaug, D. S. Schrump, W. M. Linehan, R. Roychoudhuri, N. P. Restifo, Ionic immune suppression within the tumour microenvironment limits T cell effector function. *Nature* **537**, 539–543 (2016).
7. L. A. Pardo, W. Stühmer, The roles of K⁺ channels in cancer. *Nat. Rev. Cancer* **14**, 39–48 (2013).
8. C. C. Shieh, M. Coghlan, J. P. Sullivan, M. Gopalakrishnan, Potassium channels: Molecular defects, diseases, and therapeutic opportunities. *Pharmacol. Rev.* **52**, 557–593 (2000).
9. G. R. C. Hamilton, S. K. Sahoo, S. Kamila, N. Singh, N. Kaur, B. W. Hyland, J. F. Callan, Optical probes for the detection of protons, and alkali and alkaline earth metal cations. *Chem. Soc. Rev.* **44**, 4415–4432 (2015).
10. E. H. Kim, G. Chin, G. Rong, K. E. Poskanzer, H. A. Clark, Optical probes for neurobiological sensing and imaging. *Acc. Chem. Res.* **51**, 1023–1032 (2018).
11. H. Bischof, M. Rehberg, S. Stryeck, K. Artinger, E. Eroglu, M. Waldeck-Weiermair, B. Gottschalk, R. Rost, A. T. Deak, T. Niedrist, N. Vujic, H. Lindermuth, R. Prassl, B. Pelzmann, K. Groschner, D. Kratky, K. Eller, A. R. Rosenkranz, T. Madl, N. Plesnila, W. F. Graier, R. Malli, Novel genetically encoded fluorescent probes enable real-time detection of potassium in vitro and in vivo. *Nat. Commun.* **8**, 1422 (2017).
12. T. T. Ruckh, C. G. Skipwith, W. Chang, A. W. Senko, V. Bulovic, P. O. Anikeeva, H. A. Clark, Ion-switchable quantum dot Förster resonance energy transfer rates in ratiometric potassium sensors. *ACS Nano* **10**, 4020–4030 (2016).

13. P. Padmawar, X. Yao, O. Bloch, G. T. Manley, A. S. Verkman, K⁺ waves in brain cortex visualized using a long-wavelength K⁺-sensing fluorescent indicator. *Nat. Methods* **2**, 825–827 (2005).

14. J. Wellbourne-Wood, T. S. Rimmele, J.-Y. Chatton, Imaging extracellular potassium dynamics in brain tissue using a potassium-sensitive nanosensor. *Neurophotonics* **4**, 015002 (2017).

15. X. Zhou, F. Su, Y. Tian, C. Youngbull, R. H. Johnson, D. R. Meldrum, A new highly selective fluorescent K⁺ sensor. *J. Am. Chem. Soc.* **133**, 18530–18533 (2011).

16. M. L. Gumz, L. Rabinowitz, C. S. Wingo, An integrated view of potassium homeostasis. *N. Engl. J. Med.* **373**, 60–72 (2015).

17. T. Shinoda, H. Ogawa, F. Cornelius, C. Toyoshima, Crystal structure of the sodium–potassium pump at 2.4 Å resolution. *Nature* **459**, 446–450 (2009).

18. A. Thibon, V. C. Pierre, A highly selective luminescent sensor for the time-gated detection of potassium. *J. Am. Chem. Soc.* **131**, 434–435 (2009).

19. S. Chen, A. Z. Weitemier, X. Zeng, L. He, X. Wang, Y. Tao, A. J. Y. Huang, Y. Hashimotodani, M. Kano, H. Iwasaki, L. K. Parajuli, S. Okabe, D. B. L. Teh, A. H. All, I. Tsutsui-Kimura, K. F. Tanaka, X. Liu, T. J. McHugh, Near-infrared deep brain stimulation via upconversion nanoparticle–mediated optogenetics. *Science* **359**, 679–684 (2018).

20. G. Chen, H. Qiu, P. N. Prasad, X. Chen, Upconversion nanoparticles: Design, nanochemistry, and applications in theranostics. *Chem. Rev.* **114**, 5161–5214 (2014).

21. Y. I. Park, K. T. Lee, Y. D. Suh, T. Hyeon, Upconverting nanoparticles: A versatile platform for wide-field two-photon microscopy and multi-modal in vivo imaging. *Chem. Soc. Rev.* **44**, 1302–1317 (2015).

22. B. Zhou, B. Shi, D. Jin, X. Liu, Controlling upconversion nanocrystals for emerging applications. *Nat. Nanotechnol.* **10**, 924–936 (2015).

23. M. Haase, H. Schäfer, Upconverting nanoparticles. *Angew. Chem. Int. Ed.* **50**, 5808–5829 (2011).

24. J. Liu, Y. Liu, W. Bu, J. Bu, Y. Sun, J. Du, J. Shi, Ultrasensitive nanosensors based on upconversion nanoparticles for selective hypoxia imaging in vivo upon near-infrared excitation. *J. Am. Chem. Soc.* **136**, 9701–9709 (2014).

25. J. Kim, H. S. Kim, N. Lee, T. Kim, H. Kim, T. Yu, I. C. Song, W. K. Moon, T. Hyeon, Multifunctional uniform nanoparticles composed of a magnetite nanocrystal core and a mesoporous silica shell for magnetic resonance and fluorescence imaging and for drug delivery. *Angew. Chem. Int. Ed. Engl.* **47**, 8438–8441 (2008).

26. W. Wu, A. M. Kirillov, X. Yan, P. Zhou, W. Liu, Y. Tang, Enhanced separation of potassium ions by spontaneous K⁺-induced self-assembly of a novel metal-organic framework and excess specific cation-π interactions. *Angew. Chem. Int. Ed. Engl.* **53**, 10649–10653 (2014).

27. S. Y. Noskov, S. Bernèche, B. Roux, Control of ion selectivity in potassium channels by electrostatic and dynamic properties of carbonyl ligands. *Nature* **431**, 830–834 (2004).

28. H. He, M. A. Mortellaro, M. J. P. Leiner, R. J. Fraatz, J. K. Tusa, A fluorescent sensor with high selectivity and sensitivity for potassium in water. *J. Am. Chem. Soc.* **125**, 1468–1469 (2003).

29. J. M. Dubach, S. Das, A. Rosenzweig, H. A. Clark, Visualizing sodium dynamics in isolated cardiomyocytes using fluorescent nanosensors. *Proc. Natl. Acad. Sci. U.S.A.* **106**, 16145–16150 (2009).

30. B. Pelaz, P. del Pino, P. Maffre, R. Hartmann, M. Gallego, S. Rivera-Fernández, J. M. de la Fuente, G. U. Nienhaus, W. J. Parak, Surface functionalization of nanoparticles with polyethylene glycol: Effects on protein adsorption and cellular uptake. *ACS Nano* **9**, 6996–7008 (2015).

31. M. Howarth, K. Takao, Y. Hayashi, A. Y. Ting, Targeting quantum dots to surface proteins in living cells with biotin ligase. *Proc. Natl. Acad. Sci. U.S.A.* **102**, 7583–7588 (2005).

32. A. C. Charles, S. M. Baca, Cortical spreading depression and migraine. *Nat. Rev. Neurol.* **9**, 637–644 (2013).

33. N. Hadjikhani, M. Sanchez del Rio, O. Wu, D. Schwartz, D. Bakker, B. Fischl, K. K. Kwong, F. M. Cutrer, B. R. Rosen, R. B. H. Tootell, A. G. Sorensen, M. A. Moskowitz, Mechanisms of migraine aura revealed by functional MRI in human visual cortex. *Proc. Natl. Acad. Sci. U.S.A.* **98**, 4687–4692 (2001).

34. C. Diaz Verdugo, S. Myren-Svelstad, E. Aydin, E. Van Hoeymissen, C. Deneubourg, S. Vanderhaeghe, J. Vancraeynest, R. Pelgrims, M. I. Cosacak, A. Muto, C. Kizil, K. Kawakami, N. Jurisch-Yaksi, E. Yaksi, Glia-neuron interactions underlie state transitions to generalized seizures. *Nat. Commun.* **10**, 3830 (2019).

35. A. Wallraff, R. Köhling, U. Heinemann, M. Theis, K. Willecke, C. Steinhäuser, The impact of astrocytic gap junctional coupling on potassium buffering in the hippocampus. *J. Neurosci.* **26**, 5438–5447 (2006).

36. L. Turrini, C. Fornetto, G. Marchetto, M. C. Müllenbroich, N. Tiso, A. Vettori, F. Resta, A. Masi, G. Mannaioni, F. S. Pavone, F. Vanzi, Optical mapping of neuronal activity during seizures in zebrafish. *Sci. Rep.* **7**, 3025 (2017).

37. Y. Liu, Y. Lu, X. Yang, X. Zheng, S. Wen, F. Wang, X. Vidal, J. Zhao, D. Liu, Z. Zhou, C. Ma, J. Zhou, J. A. Piper, P. Xi, D. Jin, Amplified stimulated emission in upconversion nanoparticles for super-resolution nanoscopy. *Nature* **543**, 229–233 (2017).

38. Q. Liu, Y. Zhang, C. S. Peng, T. Yang, L.-M. Joubert, S. Chu, Single upconversion nanoparticle imaging at sub-10 W cm⁻² irradiance. *Nat. Photon.* **12**, 548–553 (2018).

39. D. J. Gargas, E. M. Chan, A. D. Ostrowski, S. Aloni, M. V. P. Altoe, E. S. Barnard, B. Sanii, J. J. Urban, D. J. Milliron, B. E. Cohen, P. J. Schuck, Engineering bright sub-10-nm upconverting nanocrystals for single-molecule imaging. *Nat. Nanotechnol.* **9**, 300–305 (2014).